Exceptional point enhances sensitivity of optomechanical mass sensors

P. Djorwe, Yan Pennec, Bahram Djafari-Rouhani

Exceptional Point Enhances Sensitivity of Optomechanical Mass Sensors

P. Djorwe,* Y. Pennec, and B. Djafari-Rouhani
Institut d'Electronique, de Microélectronique et Nanotechnologie, UMR CNRS 8520 Université de Lille, Faculté des sciences et technologies, 59652 Villeneuve d'Ascq France

(Received 8 March 2019; revised manuscript received 28 June 2019; published 1 August 2019)

We propose an efficient optomechanical mass sensor operating at exceptional points (EPs), non-Hermitian degeneracies where eigenvalues of a system and their corresponding eigenvectors simultaneously coalesce. The benchmark system consists of two optomechanical cavities that are mechanically coupled, where we engineer mechanical gain (loss) by driving the cavity with a blue-detuned (red-detuned) laser. The system features an EP at the gain and loss balance, where any perturbation induces a frequency splitting that scales as the square root of the perturbation strength, resulting in a giant sensitivity-factor enhancement compared with conventional optomechanical sensors. For nonidentical mechanical resonators, quadratic optomechanical coupling is used to tune the frequency mismatch to get closer to the EP, extending the efficiency of our sensing scheme to mismatched resonators. This work paves the way toward new levels of sensitivity for optomechanical sensors, which could find applications in many other fields, including nanoparticle detection, precision measurement, and quantum metrology.

DOI: 10.1103/PhysRevApplied.12.024002

I. INTRODUCTION

Owing to rapid progress in microengineering and nanoengineering of mechanical resonators, tremendous advances have been made in mass sensing with the view of achieving ultrasensitive detection [1,2]. Resonant mass sensors are widely used in diverse fields of science and technology. For instance, they are actively used to detect single biomolecules, viruses, nanoparticles, and other nano-objects. Because of these interesting applications, nanomechanical mass sensors have attracted much attention over the last few years. This has led to detection ranging from femtograms (10^{-15} g) [3] though attograms (10^{-18} g) [4] and zeptograms (10^{-21} g) [5] to yoctograms (10^{-24} g) [6].

Besides these sensors based on electrical excitations, all-optical mass sensors have been proposed as well, with the aim of reaching new levels of sensitivity and to break through the limitation of frequency restriction (Ref. [7]). Optomechanical sensors have been revealed as excellent candidates for mass detection due to their simplicity and sensitivity and because the optical field serves both as an actuator and as a probe for precise monitoring of the mechanical frequencies. Single optomechanical sensors, exploiting nonlinearities of the systems, were proposed in Refs. [8–10], whereas coupled optomechanical cavities were used for sensing in the work reported in Refs. [11,12]. A mechanical resonator was inserted inside one of the coupled optical cavities in the work reported in Ref. [11], while a hybrid optoelectromechanical system consisting of optical and microwave cavities coupled to a common mechanical oscillator was used in the work reported in Ref. [12]. It was found that sensors based on coupled systems perform better than their counterparts based on a single cavity. This conclusion remains the same even for coupled mechanical resonators driven by a common electromagnetic field as shown in Refs. [13,14]. The main reason of such performance lies in the fact that sensitivity in coupled structures is determined through the splitting of eigenmodes, and therefore it can be significantly increased even without entering the strong coupling regime. This is not the case for electromechanical mass sensors or for the aforementioned single optomechanical mass sensors, where the sensing process tracks the frequency shifts of the mechanical resonator due to mass changes induced by any added tiny object [1,2]. Moreover, the simple multimodal response of a mechanical resonator enables mass sensing at much higher levels of accuracy than what is typically achieved with a single frequency-shift measurement [15]. It goes without saying that mass sensor performances are enhanced in coupled systems that feature a strong coupling regime or those exhibiting very narrow splitting in their eigenmode structure.

Recently, sensitivity enhancement of more than threefold in particle detection was theoretically demonstrated with a sensor operating at exceptional points (EPs) [16]. Owing to the complex square-root topology near an EP, any perturbation lifts the degeneracy, leading to a

*djorwepp@gmail.com

frequency splitting that scales as the square root of the perturbation strength. This splitting is therefore larger for sufficiently small perturbation than the splitting observed in conventional sensing schemes, where the linewidth or frequency shift or splitting is proportional to the strength of the perturbation. Later, these theoretical results were validated by two experimental studies, at an EP in a whispering-gallery-mode microtoroid cavity [17] and with a higher order EP in a parity-time-symmetric ($\mathcal{PT}$-symmetric) photonic laser molecule [18]. Along the same line, the performance of cavity-assisted metrology, where a cavity is coupled to the device under test, was enhanced near an EP in $\mathcal{PT}$-symmetric microcavities [19]. It follows that an EP is a useful tool for the next generation of sensors for reaching new levels of sensitivity.

Our proposal is based on two optomechanical cavities mechanically coupled through their moving mechanical resonators. This benchmark system has the advantage that it enables one to get an effective coupled mechanical system, where mechanical gain (loss) can be easily engineered by driving the cavity with a blue-detuned (red-detuned) laser. At the balance between gain and loss, the system features an EP in its mechanical spectrum [20], which is the key point of our EP-based optomechanical mass sensor. The proposed sensor differs from known sensors [16–19] in at least three points: (i) it operates at an EP generated on its mechanical spectrum (instead of the optical spectrum), (ii) the gain and loss are self-engineered while the cavities are driven, and (iii) it does not needs the $\mathcal{PT}$-symmetric requirement. In the vicinity of the EP, our proposed sensing scheme exhibits a giant enhancement of the sensitivity factor compared with conventional opto(electro)mechanical sensing schemes. This efficiency comes from the topological complex square root near the EP, and is highly pronounced for small perturbations. Bearing in mind the laborious microfabrication or nanofabrication task of engineering two identical mechanical resonators, we extend our results to nonidentical mechanical resonators, where their frequency mismatch can be tuned through quadratic coupling, which is well known in optomechanics [21]. This work is organized as follows. In Sec. II, the model and its dynamical equations up to the EP features are described. The sensitivity enhancement, in the vicinity of the EP for degenerate mechanical resonators, is presented in Sec. III. Section IV is devoted to the sensitivity assisted by quadratic coupling for the nonidentical case. The experimental feasibility of our proposal is presented in Sec. V, while Sec. VI concludes the work.

II. MODELING AND DYNAMICAL EQUATIONS

The system we propose is sketched in Fig. 1(a). It consists of two optomechanical cavities mechanically coupled through their moving mechanical resonators. The first cavity is driven with a red-detuned laser, while the second

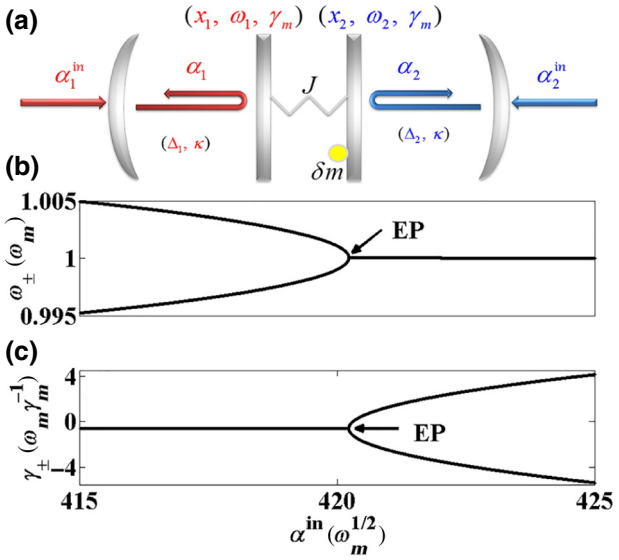

FIG. 1. (a) Generic setup. Two optomechanical cavities, one with gain (blue) and the other generating losses (red), are mechanically coupled. The yellow dot represents a deposited mass that acts as a perturbation. (b),(c) Real and imaginary parts of the eigenvalues versus the driving strength α^{in}, which depict the EP feature.

one is excited with a blue-detuned driving field. By symmetrically driving the cavities at the sidebands mentioned, we can engineer either mechanical gain or mechanical loss. In the rotating frame of the driving fields (ω_p), the Hamiltonian ($\hbar = 1$) describing this system is

$$H = H_{\rm OM} + H_{\rm int} + H_{\rm drive}, \tag{1}$$

where

$$\begin{aligned} H_{\rm OM} &= \sum\nolimits_{j=1,2} \omega_j b_j^\dagger b_j - \Delta_j a_j^\dagger a_j - g a_j^\dagger a_j (b_j^\dagger + b_j), \\ H_{\rm int} &= -J(b_1 b_2^\dagger + b_1^\dagger b_2), \\ H_{\rm drive} &= iE \sum\nolimits_{j=1,2} (a_j^\dagger - a_j). \end{aligned} \tag{2}$$

In this Hamiltonian, a_j and b_j are the annihilation bosonic field operators describing the optical and mechanical resonators, respectively. The mechanical displacements x_j are connected by b_j as $x_j = x_{\rm ZPF}(b_j + b_j^\dagger)$, where $x_{\rm ZPF}$ is the zero-point fluctuation amplitude of the mechanical resonator. The mechanical frequency of the jth resonator is ω_j, and $\Delta_j = \omega_p^j - \omega_{\rm cav}^j$ is the optical detuning between the optical frequency and the cavity frequency ($\omega_{\rm cav}^j$). The mechanical coupling strength between the two mechanical resonators is J, and the linear optomechanical coupling is g. By using the well-known optomechanical input-output formalism [22], one can derive from the above Hamiltonian

the quantum Langevin equations (QLEs) for both the cavity field amplitudes a_j and the mechanical amplitude b_j. In the limit of large photon number, the mean values of the operators can be treated as classical variables. Hence, after our setting the mean values of the operators as $\langle a_j \rangle = \alpha_j$ for the optics and $\langle b_j \rangle = \beta_j$ for the mechanics, the classical set of nonlinear equations of our system yields [22]

$$\begin{aligned} \dot{\alpha}_j &= \left\{ i\left[\Delta_j + g\left(\beta_j^* + \beta_j\right)\right] - \frac{\kappa}{2} \right\} \alpha_j + \sqrt{\kappa}\alpha^{\text{in}}, \\ \dot{\beta}_j &= -\left(i\omega_j + \frac{\gamma_m}{2}\right)\beta_j + iJ\beta_{3-j} + ig\alpha_j^*\alpha_j, \end{aligned} \tag{3}$$

where optical (κ) and mechanical ($\gamma_j \equiv \gamma_m$) dissipations have been added, and the amplitude of the driving pump has been substituted as $E = \sqrt{\kappa}\alpha^{\text{in}}$ to account for losses. In this form, the input laser power P_{in} acts through $\alpha^{\text{in}} = \sqrt{P_{\text{in}}/\hbar\omega_p}$, which is the same power used to drive symmetrically both mechanical resonators. Without loss of generality, the parameters γ_m, g, and κ are assumed to be degenerate for the whole system. Moreover, they follows the hierarchy $\gamma_m, g \ll \kappa \ll \omega_m$, as encountered in resolved-sideband-regime experiments [23,24].

To investigate the sensitivity performance of the proposed sensor, we need to compute the eigenvalues of the effective mechanical system to identify the EP feature. One can obtain this effective system by integrating $\alpha_j(t)$ out of the full set of Eq. (3). This can be straightforwardly done by approaching the mechanical oscillations with the ansatz $\beta_j(t) = \bar{\beta}_j + A_j \exp(-i\omega_{\text{lock}}t)$ (see Ref. [20] for more details), where $\bar{\beta}_j$ is a constant shift in the origin of the movement, A_j is the slowly-time-dependent amplitude, and ω_{lock} is the mechanical degenerate frequency when the resonators experience frequency locking. This leads to the following mechanical effective Hamiltonian:

$$H_{\text{eff}} = \begin{pmatrix} \omega_{\text{eff}}^1 - i\dfrac{\gamma_{\text{eff}}^1}{2} & -J \\ -J & \omega_{\text{eff}}^2 - i\dfrac{\gamma_{\text{eff}}^2}{2} \end{pmatrix}, \tag{4}$$

having the eigenvalues

$$\lambda_\pm = \frac{\omega_{\text{eff}}^1 + \omega_{\text{eff}}^2}{2} - \frac{i}{4}\left(\gamma_{\text{eff}}^1 + \gamma_{\text{eff}}^2\right) \pm \frac{\sigma}{4}, \tag{5}$$

with

$$\sigma = \sqrt{16J^2 + [2(\omega_{\text{eff}}^1 - \omega_{\text{eff}}^2) + i(\gamma_{\text{eff}}^2 - \gamma_{\text{eff}}^1)]^2}. \tag{6}$$

Here $\omega_{\text{eff}}^j = \omega_m + \delta\omega_{\text{opt}}^j$ and $\gamma_{\text{eff}}^j = \gamma_m + \gamma_{\text{opt}}^j$ are the effective frequencies and dampings, respectively. Furthermore, $\delta\omega_{\text{opt}}^j$ and γ_{opt}^j are the optical spring effect and the optical damping induced by the optical fields, respectively. These terms are given as

$$\delta\omega_{\text{opt}}^j = -\frac{2\kappa(g\alpha^{\text{in}})^2}{\omega_{\text{lock}}\epsilon_j}\text{Re}\left(\sum_n \frac{J_{n+1}(-\epsilon_j)J_n(-\epsilon_j)}{h_{n+1}^{j*}h_n^j}\right) \tag{7}$$

and

$$\gamma_{\text{opt}}^j = \frac{2(g\kappa\alpha^{\text{in}})^2}{\epsilon_j}\sum_n \frac{J_{n+1}(-\epsilon_j)J_n(-\epsilon_j)}{\left|h_{n+1}^{j*}h_n^j\right|^2}, \tag{8}$$

where $\epsilon_j = 2g\text{Re}\,A_j/\omega_{\text{lock}}$ is a normalized amplitude, J_n is the Bessel function, $h_n^j = i\left(n\omega_{\text{lock}} - \tilde{\Delta}_j\right) + \kappa/2$, and $\tilde{\Delta}_j = \Delta_j + 2g(\bar{\beta}_j)$ is the effective detuning [20]. The eigenfrequencies and the dampings of the system are defined as the real ($\omega_\pm = \text{Re}\,\lambda_\pm$) and imaginary ($\gamma_\pm = \text{Im}\,\lambda_\pm$) parts of $\lambda_\pm$, respectively.

At the EP, both these pairs of frequencies and dampings coalesce, $\omega_- = \omega_+ \equiv \omega_{\text{lock}}$ and $\gamma_- = \gamma_+$. From Eq. (5), this is equivalent to $\sigma = 0$, which requires control of the real and imaginary parts of σ through the driving fields (α_j^{in}) and detunings (Δ_j) [25]. For a proof of concept of the proposed sensor, we assume in the next section that the two mechanical resonators are degenerate ($\omega_j \equiv \omega_m$). The nonidentical case, where there is a frequency mismatch due to microfabrication or nanofabrication imperfections, for instance, is discussed in Sec. IV.

III. SENSITIVITY AT THE EXCEPTIONAL POINT

The eigenvalues of our effective mechanical system undergo a singularity (known as an EP) in their spectrum as shown in Figs. 1(b) and 1(c). The efficiency of the proposed sensor depends on this EP, which emerges from the eigenvalues given in Eq. (5), instead of tracking the resonant-frequency shift induced by mass deposition on the surface of the resonators [8–13]. For an ordinary mass sensor, the relationship between the frequency shift $\delta\omega$ and the deposited mass δm is given by [1,2]

$$\delta m = \frac{2m}{\omega_m}\delta\omega = \mathcal{R}^{-1}\delta\omega, \tag{9}$$

where $\mathcal{R} = \omega_m/2m$ stands for the mass responsivity and m is the mass of the resonator supporting the deposition. The induced frequency shift is proportional to the strength of the perturbation. At the EP, both frequencies ($\omega_\pm$) and dampings ($\gamma_\pm$) coalesce [see Fig. 1(b)], and any external perturbation will split these eigenvalues, leading to high sensitivity (see Fig. 3). To gain insight into this feature, we assume that a mass [see the yellow dot in Fig. 1(a)] has been deposited on the mechanical resonator driven by the blue-detuned field ($m_2 \equiv m$), which will induce its resonance to shift according to Eq. (9). As the resonators are

coupled, this localized shift will affect the whole system, resulting in a splitting at the EP. For degenerate resonators, and for the weak driving regime, one has $\delta\omega^{j}_{\rm opt} \ll \omega_m$, and Eq. (5) simplifies to

$$\lambda_{\pm} \approx \omega_m - \frac{i}{4}\left(\gamma^1_{\rm eff} + \gamma^2_{\rm eff}\right) \pm \sqrt{J^2 - \left(\frac{\Delta\gamma_{\rm eff}}{4}\right)^2}, \quad (10)$$

where $\Delta\gamma_{\rm eff} = \gamma^2_{\rm eff} - \gamma^1_{\rm eff}$. As the second resonator experiences a small perturbation δm (or shift $\delta\omega$), this affects the eigenvalues as (see Appendix A)

$$\lambda^{\delta\omega}_{\pm} \approx \omega_m + \frac{\delta\omega}{2} - \frac{i}{4}\left(\gamma^1_{\rm eff} + \gamma^2_{\rm eff}\right) \pm \sqrt{J^2 - \left(\frac{\Delta\gamma_{\rm eff}}{4}\right)^2 + \frac{\delta\omega^2 + i\delta\omega\Delta\gamma_{\rm eff}}{4}}. \quad (11)$$

This perturbation generally affects also the optical dampings, but for the sake of a qualitative discussion and since the corresponding variations are very small [see Figs. 6(a) and 6(b) in Appendix A], we do not include them in Eq. (11). However, it is worth noting that these effects are fully accounted for in our simulated results. We define sensitivity as the frequency shift of a supermode relative to its reference signal; that is, the frequency splitting of these two pairs of supermodes $\mathrm{Re}\,\Delta\lambda_+ \equiv \mathrm{Re}(\lambda^{\delta\omega}_+ - \lambda_+)$ and $\mathrm{Re}\,\Delta\lambda_- \equiv \mathrm{Re}(\lambda^{\delta\omega}_- - \lambda_-)$ as shown in Figs. 2(a) and 2(b). Significant splitting is experienced at the EP [see Fig. 2(a)], resulting in high sensitivity $|\mathrm{Re}\,\Delta\lambda|$ as depicted in Fig. 2(b). This feature can be approached through our aforementioned analytical investigation. Indeed, the system has an EP when $4J = \Delta\gamma_{\rm eff}$ [see Eq. (10)]. At this degeneracy point, and from Eqs. (10) and (11), the splitting of the two pairs of supermodes can be deduced as (see Appendix A)

$$\Delta\lambda^{\rm EP} = \frac{1}{2}\left(\delta\omega \pm \sqrt{\delta\omega^2 - i\delta\omega\Delta\gamma_{\rm eff}}\right). \quad (12)$$

As expected, Eq. (12) shows that there is no splitting at the EP for $\delta\omega = 0$. For any perturbation however ($\delta\omega \neq 0$), it reveals that the two pairs of supermodes experience different splittings, $\mathrm{Re}\,\Delta\lambda_+ \neq \mathrm{Re}\,\Delta\lambda_-$, as shown in Fig. 2(b). This asymmetry depends on which resonator the extra masslike perturbation has landed. By adding the mass on the other resonator instead, we verify that the sensitivities of the supermodes are reversed. For small-enough landed mass ($|\delta\omega| \ll |\Delta\gamma_{\rm eff}|$), both pairs of supermodes experience the same amount of splitting, approximately $\sqrt{(\delta\omega\Delta\gamma_{\rm eff})/8}$ (see Appendix A). The splitting at the EP scales as the square root of the strength of the perturbation (approximately $\delta\omega^{1/2}$), in stark contrast with the linear dependence for the conventional sensors [see Eq. (9)]. Owing to this complex square-root topology near

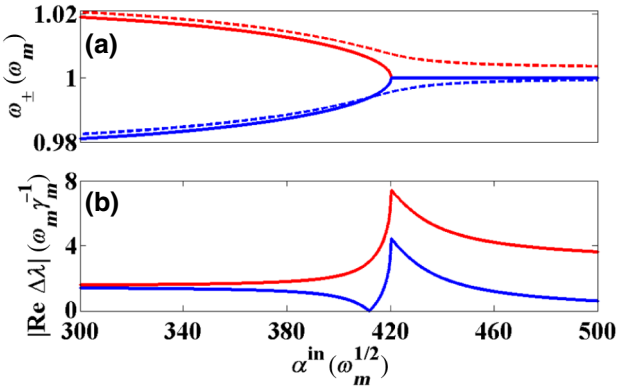

FIG. 2. (a) Frequencies of the effective mechanical system before perturbation (full lines) and after perturbation (dashed lines) by a mass deposition corresponding to a frequency shift of $\delta\omega = 2\times10^{-3}\omega_m$. (b) Gap difference between the perturbed and reference frequencies shown in (a). These quantities are plotted versus the driving strength $\alpha^{\rm in}$. Note the difference in the units on the y axis in (a),(b).

the EP, the EP sensors perform better in detecting small mass deposition than the conventional sensors. In this weak-perturbation limit, the splitting at the EP can be expressed in terms of the deposited mass as approximately $\sqrt{(\omega_m\delta m\Delta\gamma_{\rm eff})/16m}$. From this expression and Eq. (9), we can define the sensitivity enhancement factor as

$$\eta \equiv \left|\frac{\mathrm{Re}\,\Delta\lambda^{\rm EP}}{\delta\omega}\right| = \sqrt{\frac{\Delta\gamma_{\rm eff}}{8\delta\omega}} = \sqrt{\frac{m\Delta\gamma_{\rm eff}}{4\omega_m\delta m}}, \quad (13)$$

which again highlights the square-root dependence on δm, instead of a linear dependence, for small-mass deposition. Figure 3(a) shows the expected square-root-like evolution of the sensitivity versus perturbation ($\left|\mathrm{Re}\,\Delta\lambda^{\rm EP}\right| \propto \delta\omega^{1/2}$), which is revealed through the log-log-scale representation in the inset. Hence, a slope of $\frac{1}{2}$ is shown for weak perturbations, which evolves toward a 1-minus-slope behavior as the perturbation increases. This simply reveals that the sensitivity of the EP sensor scales linearly with the strength of the perturbations when they are large enough. This is confirmed through the enhancement factor η depicted in Fig. 3(b), where it evolves toward the limit $\eta \sim 1$ for strong-enough perturbation. It can also be seen that η is greatly increased for weak perturbation strength [see the inset in Fig. 3(b)], proving the efficiency of the EP sensor in detecting small particles, mass, or objects.

Another interesting feature of EP sensors is that they have improved linewidth performance as well. As the linewidths are also degenerate at the EP, adding extra mass will also lift this degeneracy. This is depicted in Fig. 4(a), and the corresponding sensitivity is shown in Fig. 4(b). In contrast to Fig. 2(b), here both sensitivities given by the pairs of supermodes are the same. This can

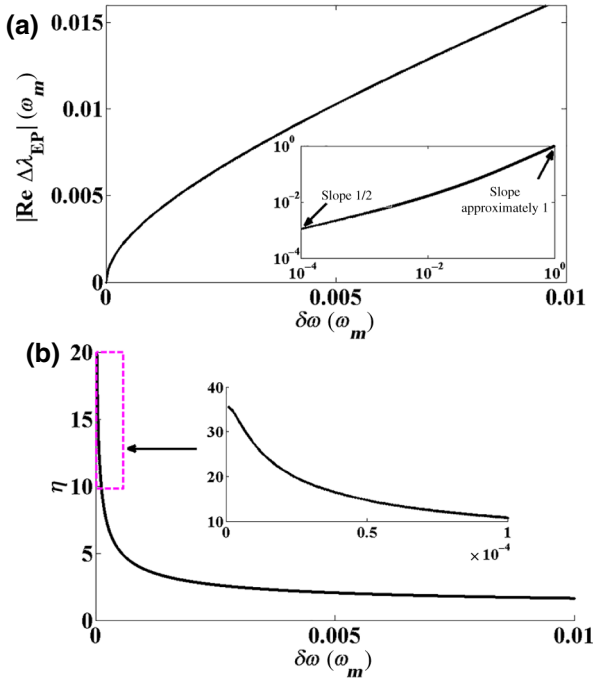

FIG. 3. (a) Sensitivity at the exceptional point versus the strength of the perturbation $\delta\omega$. The inset shows a log-log-scale representation. (b) Enhancement factor η versus $\delta\omega$. It can be seen that for weak perturbation (see the inset) the EP sensor performs better, and it has the same performance as the conventional sensors as the perturbation increases.

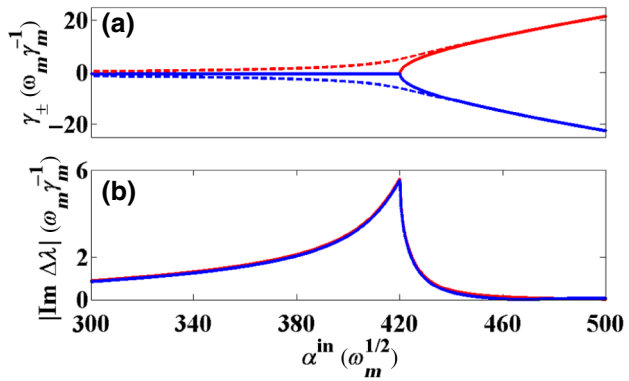

FIG. 4. (a) Dampings as reference (full lines) and perturbed (dashed lines), with the associated splittings in (b). These plots are versus the driving strength α^{in}.

be expected by referring to the imaginary part of Eq. (12) as given in Appendix A. By further driving of the system, the linewidths move out of the vicinity of the EP, and one of them grows, whereas the other decays. This simply means that one supermode experiences gain, while the other experiences loss.

IV. ENHANCING SENSITIVITY THROUGH QUADRATIC COUPLING

In the previous section we dealt with an EP-based optomechanical sensor, where the coupled mechanical resonators are degenerate. However, engineering such identical resonators is not often a simple task with microfabrication and nanofabrication technologies. Therefore, any mismatch between the mechanical resonance frequencies will lift the EP degeneracy, impairing the performance of the proposed sensor. It could be interesting to extend the detection process studied in the previous section to a system composed of nonidentical resonators. This can break through the limitation of microfabrication and nanofabrication restriction, and will pave the way toward EP sensors that are robust to defects or fabrication imperfections. One way to go beyond this technological limitation is to engineer nonlinearities to control and compensate the frequency mismatch. Such optical control of frequency was recently investigated to enhance energy transfer between two nonidentical mechanical resonators [26,27]. Duffing nonlinearity was used in the work reported in Ref. [26], whereas an optical trapping coupling was used in the work reported in Ref. [27] to trap the mechanical motion. Although these techniques resulted in an efficient transfer around the avoided crossing level, this was still not enough to induce an EP feature in the system. The reason is that the strong coupling observed in these studies leads to level repulsion, gap opening between two modes due to coupling, while the EP arises from a level-attraction process instead [28]. To reach our goal, we propose a position-squared coupling where the optical mode is coupled in a quadratic fashion to the mechanical motion [21]. This can be engineered by optically trapping the second resonator (β_2) inside the cavity driven on the blue sideband, which could have been achieved in the work reported in Ref. [27] as well. The resulting cross-Kerr-interaction is described by the Hamiltonian $H_{\text{cK}} = -g_{\text{cK}} a_2^\dagger a_2 b_2^\dagger b_2$, which has to be accounted for in Eq. (1) for a full corresponding model. From the corresponding full Hamiltonian, we follow the same input-output formalism as before to derive the QLEs for the cavity field a_j and for the mechanical amplitude b_j. In the limit of large photon number, the classical variables are deduced ($\langle a_j \rangle = \alpha_j$, $\langle b_j \rangle = \beta_j$), leading to the optically tunable mechanical frequency $\tilde{\omega_2} = \omega_2 - g_{\text{cK}}\alpha_2^*\alpha_2$ (see Appendix B for more details). By assuming that the coupled mechanical resonators fulfill the condition $\omega_2 > \omega_1$, and for a given cross-Kerr-term $g_{\text{cK}} > 0$, one can optically adjust the effective frequencies to satisfy $\omega_{\text{eff}}^1 \sim \omega_{\text{eff}}^2$, which is a good requirement for the EP as presented above. Therefore, cross-Kerr-coupling is useful not only to engineer an EP in nonidentical coupled resonators, but it also enables one to enhance the performance of an EP-based optomechanical sensor for a mismatched set of resonators, regardless of their technological imperfections. Figure 5(a) shows the frequency-control strategy in $(\alpha^{\text{in}}, g_{\text{cK}})$ space for a given frequency mismatch $\nu = \omega_2 - \omega_1 = 2 \times 10^{-3}\omega_m$.

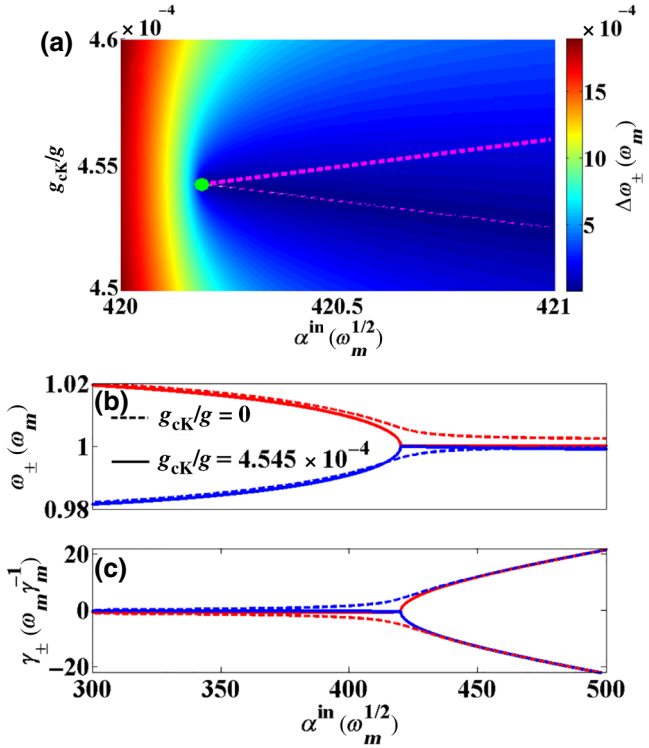

FIG. 5. (a) The control strategy in (α^{in}, g_{cK}) space at a fixed frequency mismatch $\nu = 2 \times 10^{-3}\omega_m$. (b),(c) Eigenvalues corresponding to the green dot in (a), where we see an EP feature induced by the control strategy. The dashed lines correspond to the case without control ($g_{cK}/g = 0$), whereas the control has been applied ($g_{cK}/g = 4.545 \times 10^{-4}$) for the solid lines.

It can be seen that any mismatch ($\nu \neq 0$) requires a corresponding cross-Kerr-value to reach the minimal splitting $\Delta\omega_\pm$ [see the color bar in Fig. 5(a)], which is depicted by the dashed magenta line for a given couple of parameters (α^{in}, g_{cK}). The eigenvalues that correspond to the green dot in Fig. 5(a) are represented in Fig. 5(b), where we can see the efficiency of the strategy control as well as the EP feature. The dashed lines correspond to the case without control ($g_{cK}/g = 0$), whereas the control is applied ($g_{cK}/g = 4.545 \times 10^{-4}$) for the solid lines. The observed large splitting in the case without control reveals the absence of an EP together with the fact that a small object cannot be efficiently detected. Therefore, a position-squared coupling is a useful tool to tune nonidentical mechanical resonators closer to their EP. Hence, detection of an EP-based optomechanical sensor can be enhanced through quadratic coupling, resulting in a giant sensitivity factor compared with the conventional sensors.

V. EXPERIMENTAL FEASIBILITY

Owing to recent progress in nanofabrication, our proposed EP-based mass sensor can be experimentally tested. An optomechanical circuit consisting of two optomechanical crystal cavities connected by a phonon waveguide

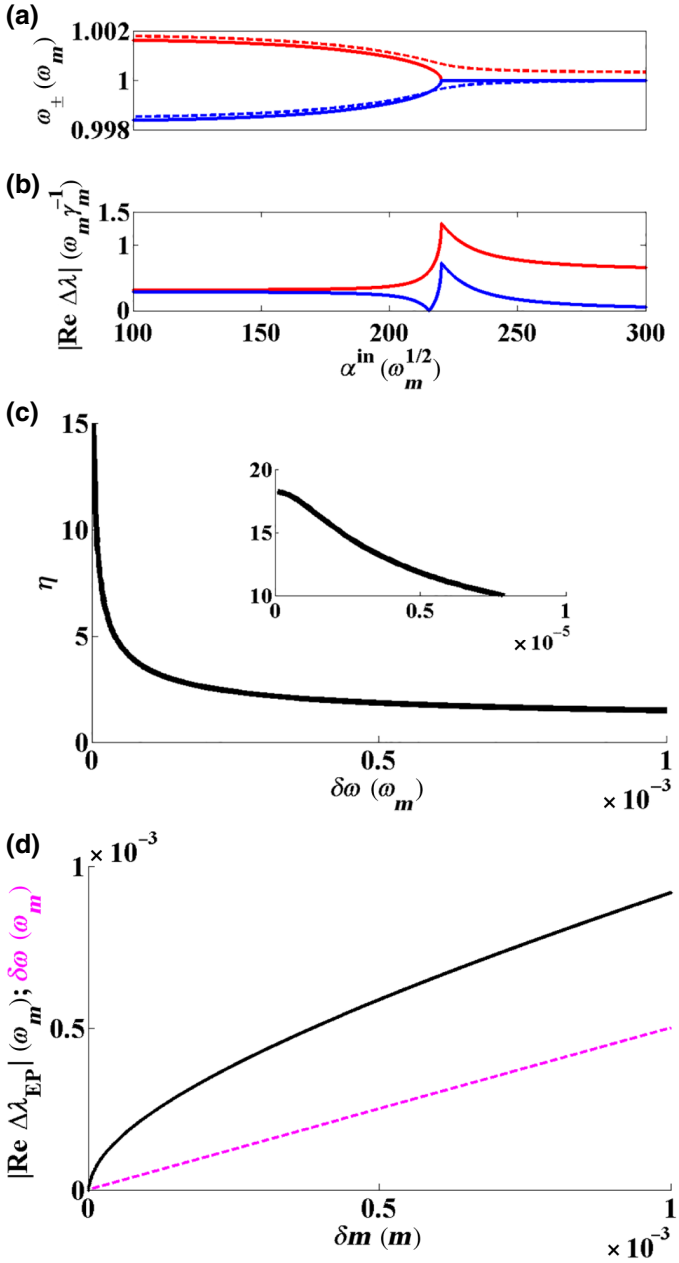

FIG. 6. (a) Eigenfrequencies before perturbation (full curve) and after perturbation (dashed curve) by a mass deposition inducing a frequency shift of $\delta\omega = 3 \times 10^{-4}\omega_m$. (b) Gap difference between the perturbed and reference frequencies shown in (a). (c) Enhancement factor η versus $\delta\omega$. (d) Frequency splitting at the exceptional point (full line) and frequency shift for a conventional sensing scheme (dashed line) versus the mass deposition δm. These results correspond to the experimental parameters in Ref. [29].

was recently investigated [29]. Such a circuit that has been used both for optical transduction and for routing of phonons constitutes a nice benchmark to test our proposal. Moreover, this system can be used to store phonons among different nodes under the control of driving laser

fields, providing various platforms for phonon information processing. To bridge the theoretical proposal and experiments, we use the following practical device parameters [29]: $\omega_m/2\pi = 6$ GHz, $\gamma_m/2\pi = 3$ MHz, $g/2\pi = 0.8$ MHz, $\kappa/2\pi = 2$ GHz, and $J/2\pi = 10$ MHz. Using these parameters for the degenerate case of optomechanical cavities, as we showed in Sec. III, our aim is to reveal the feature of the EP and to demonstrate the sensing enhancement at this EP. Figures 6(a) and 6(b) faithfully reproduce the eigenfrequencies and the corresponding sensitivities, respectively, when the experimental values from Ref. [29] are used. One can identify the EP feature that appears for low driving strength $\alpha^{\text{in}} \approx 2.2 \times 10^2 \omega_m^{1/2}$, while comparing with the driving strength at which EP happens in Fig. 2(a). We also highlight that the dashed line in Fig. 6(a) results from a perturbation of $\delta\omega = 3 \times 10^{-4}\omega_m$, which is a reasonable value to be observed experimentally. This perturbation leads to the sensitivity shown in Fig. 6(b). For practical purposes, the detected perturbation must be quantified in terms of the deposited mass δm rather than the induced frequency shift $\delta\omega$. To this end, one refers to Eq. (9), which sets a clear relationship between the induced frequency shift and the deposited mass as $\delta\omega/\omega_m \equiv \delta m/2m$. Both the sensitivity and the enhancement factor can be easily represented versus either $\delta\omega$ (ω_m) or δm (m). A given frequency shift of $\delta\omega = 3 \times 10^{-4}\omega_m$ for instance, as used in Figs. 6(a) and 6(b), corresponds to a mass deposition of $\delta m = 6 \times 10^{-4} m$. Therefore, for a femtogram ($m \sim 10^{-15}$ g) mechanical resonator [30], a mass deposition (δm) of about $10^{-18}10^{-19}$ g can be detected, which is around attogram mass sensing performance. Moroever, the enhancement factor (of more than 10) depicted in Fig. 6(c) shows that our sensing scheme can detect up to a few-zeptogram mass ($\delta m \sim 10^{-21}$ g) [see the inset in Fig. 6(c)]. Furthermore, Fig. 6(c) confirms the performance of our proposal for small mass, since η is large for weak perturbation [see the inset in Fig. 6(c)] and evolves toward 1 for strong perturbation. This reveals that our proposal reaches the same sensitivity as the conventional mass sensors when the perturbation is strong enough. The performance of our proposed scheme is further revealed in Fig. 6(d), where the frequency splitting or shift is represented versus the mass deposition. The dashed magenta curve is the induced frequency shift from the conventional mass sensor [Eq. (9)], while the full black line represents the frequency splitting resulting from our scheme [Eq. (12)]. It can be clearly seen that the EP-based optomechanical mass sensor performs better, and provides a way toward new levels of sensitivity for optomechanical sensors.

VI. CONCLUSION

We propose an EP-based optomechanical mass sensor. The benchmark system is a mechanically coupled optomechanical system, where gain (loss) is engineered by our driving the cavity with a blue-detuned (red-detuned) electromagnetic field. Degeneracy known as an EP shows up in the system when the gain balances the losses, and any perturbation leads to a frequency splitting that scales as the square root of the perturbation strength, which greatly enhances the detection compared with the conventional optomechanical sensors. To break through the limitation of microfabricatiuon and nanofabrication technology restriction, we extend the performance of the proposed sensor to nonidentical mechanical resonators by using quadratic optomechanical coupling to tune the mismatch of the mechanical frequencies. Therefore, our sensing scheme is robust regardless of the technological limitation related to the engineering of mechanical resonators, and can be applied to a versatile set of resonators. Moreover, this scheme does not require a $\mathcal{PT}$-symmetric prerequisite, and can be extended to a plethora of systems, including, hybrid optoelectromechanical and superconducting microwave resonators.

ACKNOWLEDGMENT

This work was supported by the European Commission FET Open Horizon 2020 project PHENOMEN under Grant Agreement No. 713450.

APPENDIX A: CALCULATION DETAILS RELATED TO THE SENSITIVITY AND ITS ENHANCEMENT FACTOR

In the main text [see Eqs. (5) and (6)] we give the eigenvalues of our effective reduced mechanical system as

$$\lambda_{\pm} = \frac{\omega_{\text{eff}}^1 + \omega_{\text{eff}}^2}{2} - \frac{i}{4}\left(\gamma_{\text{eff}}^1 + \gamma_{\text{eff}}^2\right) \pm \frac{\sigma}{4}, \tag{A1}$$

where

$$\sigma = \sqrt{16J^2 + [2(\omega_{\text{eff}}^1 - \omega_{\text{eff}}^2) + i(\gamma_{\text{eff}}^2 - \gamma_{\text{eff}}^1)]^2}, \tag{A2}$$

where $\omega_{\text{eff}}^j = \omega_m + \delta\omega_{\text{opt}}^j$ and $\gamma_{\text{eff}}^j = \gamma_m + \gamma_{\text{opt}}^j$ are the effective frequencies and dampings, respectively. Any perturbation (δm) of the second mechanical resonator (without loss of generality) induces a frequency shift ($\delta\omega$) that affects the eigenvalues as

$$\lambda_{\pm}^{\delta\omega} = \frac{\sum_{j=1,2}\omega_j + \sum_{j=1,2}\delta\omega_{\text{opt}}^j + \delta\omega}{2} - \frac{i}{4}\left(\gamma_{\text{eff}}^1 + \gamma_{\text{eff}}^2\right) \pm \frac{\sigma^{\delta\omega}}{4}, \tag{A3}$$

where

$$\sigma^{\delta\omega} = \sqrt{16J^2 + \left[2\chi + i(\gamma_{\text{eff}}^2 - \gamma_{\text{eff}}^1)\right]^2}, \tag{A4}$$

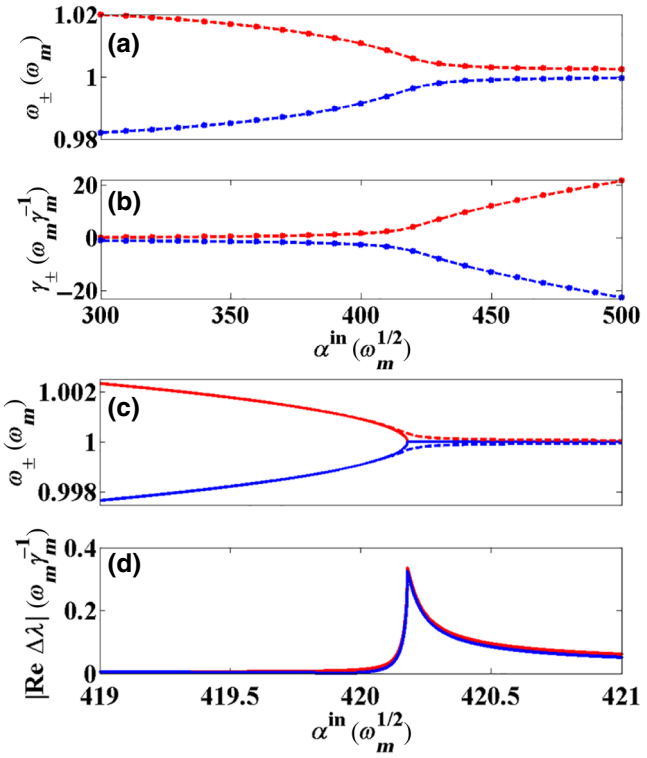

FIG. 7. (a),(b) Real and imaginary parts of the eigenvalues versus the driving field for a perturbation $\delta\omega = 2\times10^{-3}\omega_m$. The dashed lines are the numerical results, while the dotted lines represent the analytical approximation given in Eqs. (11) and (A5). This validates the approximations made in our calculations. (c),(d) Eigenfrequencies and the corresponding sensitivities for a weak perturbation $\delta\omega = 10^{-5}\omega_m$. Both frequencies experience the same sensitivity as predicted in our calculations.

where $\chi = \left(\omega_1 - \omega_2 + \delta\omega^1_{\mathrm{opt}} - \delta\omega^2_{\mathrm{opt}} - \delta\omega\right)$, and we have localized the effect of $\delta\omega$ only on the frequencies since it weakly affects the dampings [see Figs. 7(a) and 7(b)]. However, the full effect is accounted for in our numerical results given in the main text. For degenerate mechanical resonators ($\omega_j \equiv \omega_m$) and in a weak driving regime($\delta\omega^j_{\mathrm{opt}} \ll \omega_m$), Eq. (A3) can be simplified as

$$\begin{aligned}\lambda_\pm^{\delta\omega} &= \omega_m + \frac{\delta\omega}{2} - \frac{i}{4}\left(\gamma^1_{\mathrm{eff}} + \gamma^2_{\mathrm{eff}}\right)\\ &\quad \pm \frac{1}{4}\sqrt{16J^2 + \left[-2\delta\omega + i(\gamma^2_{\mathrm{eff}} - \gamma^1_{\mathrm{eff}})\right]^2}\\ &= \omega_m + \frac{\delta\omega}{2} - \frac{i}{4}\left(\gamma^1_{\mathrm{eff}} + \gamma^2_{\mathrm{eff}}\right)\\ &\quad \pm \sqrt{J^2 - \left(\frac{\Delta\gamma_{\mathrm{eff}}}{4}\right)^2 + \frac{\delta\omega^2 - i\delta\omega\Delta\gamma_{\mathrm{eff}}}{4}}. \end{aligned} \tag{A5}$$

The sensitivity is measured by the detected change between the perturbed and the nonperturbed eigenvalues. From Eq. (A5), one can deduce such quantities, providing

$$\begin{aligned}\lambda_\pm^{\delta\omega} - \lambda_\pm &= \frac{\delta\omega}{2} \pm \sqrt{J^2 - \left(\frac{\Delta\gamma_{\mathrm{eff}}}{4}\right)^2 + \frac{\delta\omega^2 - i\delta\omega\Delta\gamma_{\mathrm{eff}}}{4}}\\ &\quad \mp \sqrt{J^2 - \left(\frac{\Delta\gamma_{\mathrm{eff}}}{4}\right)^2}. \end{aligned} \tag{A6}$$

As we seek to evaluate the sensitivity of our sensor at the EP where the quantity given in Eq. (A6) has the optimal value, we use the condition $4J = \Delta\gamma_{\mathrm{eff}}$, which leads to

$$\begin{aligned}\lambda_\pm^{\mathrm{EP}} \equiv \left(\lambda_\pm^{\delta\omega} - \lambda_\pm\right)^{\mathrm{EP}} &= \frac{\delta\omega}{2} \pm \sqrt{\frac{\delta\omega^2 - i\delta\omega\Delta\gamma_{\mathrm{eff}}}{4}}\\ &= \frac{1}{2}\left(\delta\omega \pm \sqrt{\delta\omega^2 - i\delta\omega\Delta\gamma_{\mathrm{eff}}}\right). \end{aligned} \tag{A7}$$

To ease our qualitative interpretations of the physics behind Eq. (A7), it is convenient to explicitly split it into real and imaginary parts. The square root of the complex term in Eq. (A7) can be found by first converting it to polar form and then using de Moivre's theorem. After a few calculations, we straightforwardly get

$$\mathrm{Re}\,\lambda_\pm^{\mathrm{EP}} = \frac{1}{2}\left(\delta\omega \pm \sqrt{\frac{\delta\omega^2}{2} + \frac{\delta\omega}{2}\sqrt{\delta\omega^2 + \Delta\gamma^2_{\mathrm{eff}}}}\right) \tag{A8}$$

and

$$\mathrm{Im}\,\lambda_\pm^{\mathrm{EP}} = \pm\frac{1}{2}\sqrt{\frac{\delta\omega}{2}\sqrt{\delta\omega^2 + \Delta\gamma^2_{\mathrm{eff}}} - \frac{\delta\omega^2}{2}}. \tag{A9}$$

From Eqs. (A8) and (A9), we can straightforwardly deduce the sensitivities $\left|\mathrm{Re}\,\lambda_\pm^{\mathrm{EP}}\right|$ and $\left|\mathrm{Im}\,\lambda_\pm^{\mathrm{EP}}\right|$, which are depicted in Fig. 2(b) [or Fig. 3(a)] and Fig. 4(a), respectively. Moreover, Eq. (A8) reveals that the sensitivities given by the two eigenfrequencies are not equal in general, whereas the dampings result in the same sensitivity through Eq. (A9). Furthermore, Eqs. (A8) and (A9) show that the sensitivity resulting from the dampings is generally less than that coming from the eigenfrequencies $\left(\left|\mathrm{Im}\,\lambda_\pm^{\mathrm{EP}}\right| \le \left|\mathrm{Re}\,\lambda_\pm^{\mathrm{EP}}\right|\right)$. These qualitative explanations are revealed through Figs. 2(b) and 4(b).

In the weak-perturbation limit ($|\delta\omega| \ll |\Delta\gamma_{\mathrm{eff}}|$), Eqs. (A8) and (A9) are further simplified and result in approximately the identical sensitivity through approximately $\pm\sqrt{(\delta\omega\Delta\gamma_{\mathrm{eff}})/8}$ and approximately $\pm i\sqrt{(\delta\omega\Delta\gamma_{\mathrm{eff}})/8}$, respectively. In this limit, the sensitivity enhancement

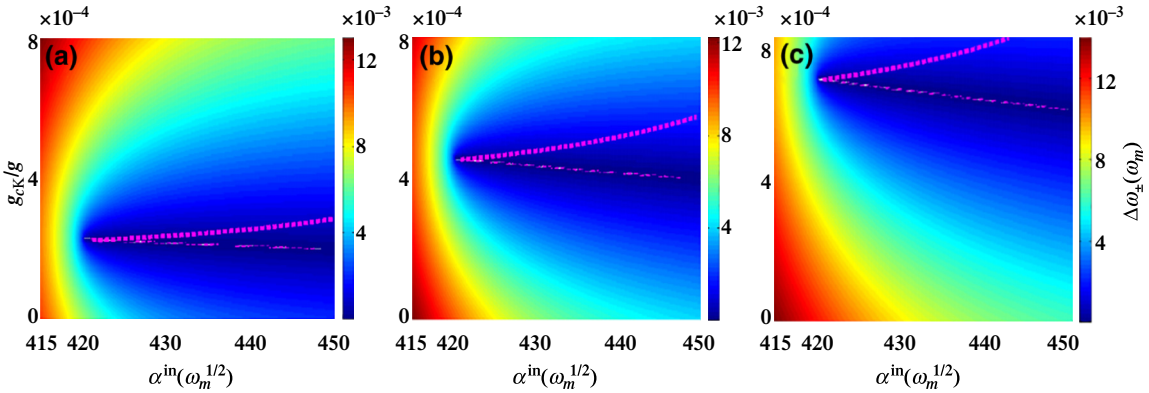

FIG. 8. Diagrams showing the control strategy in (α^{in}, g_{cK}) space, at the frequency mismatches $\nu = 1 \times 10^{-3}\omega_m$, $\nu = 2 \times 10^{-3}\omega_m$, and $\nu = 3 \times 10^{-3}\omega_m$, for (a),(b),(c) respectively. A large frequency mismatch requires a large cross-Kerr-term to reach minimal splitting.

factor η is given by

$$\eta \equiv \left|\frac{\mathrm{Re}\,\Delta\lambda_{\pm}^{EP}}{\delta\omega}\right| = \sqrt{\frac{\Delta\gamma_{\mathrm{eff}}}{8\delta\omega}} = \sqrt{\frac{m\Delta\gamma_{\mathrm{eff}}}{4\omega_m\delta m}}. \tag{A10}$$

For a given weak perturbation $\delta\omega = 10^{-5}\omega_m$, Figs. 7(c) and 7(d) show the eigenfrequencies and their corresponding sensitivities. It can be seen that the resulting sensitivities are similar for both eigenfrequencies as expected from our analysis. We underline that in the main text we used $\lambda^{EP} \equiv \lambda_{\pm}^{EP}$ to simplify our notation.

APPENDIX B: FREQUENCY CONTROL THROUGH QUADRATIC COUPLING

By our accounting for the quadratic coupling in the model, the Hamiltonian becomes

$$H = H_{\mathrm{OM,cK}} + H_{\mathrm{int}} + H_{\mathrm{drive}}, \tag{B1}$$

and

$$\begin{aligned} H_{\mathrm{OM,cK}} &= \sum_{j=1,2}\Big[\omega_j b_j^\dagger b_j - \Delta_j a_j^\dagger a_j \\ &\quad - g a_j^\dagger a_j (b_j^\dagger + b_j)\Big] - g_{\mathrm{cK}} a_2^\dagger a_2 b_2^\dagger b_2, \\ H_{\mathrm{int}} &= -J(b_1 b_2^\dagger + b_1^\dagger b_2), \\ H_{\mathrm{drive}} &= iE\sum_{j=1,2}(a_j^\dagger - a_j). \end{aligned} \tag{B2}$$

As for the case previously discussed, here we still use the input-output formalism to derive the QLEs from the full Hamiltonian given in Eq. (B2). From these QLEs, together with the requirement of large photon number in the cavities, one can treat the mean values of the operators as classical variables. This leads to the following classical set of nonlinear equations:

$$\begin{aligned} \dot{\alpha}_1 &= \left\{i\left[\Delta_1 + g\left(\beta_1^* + \beta_1\right)\right] - \frac{\kappa}{2}\right\}\alpha_1 + \sqrt{\kappa}\alpha^{\mathrm{in}}, \\ \dot{\alpha}_2 &= \left\{i\left[\Delta_2 + g\left(\beta_2^* + \beta_2\right) + g_{\mathrm{cK}}\beta_2^*\beta_2\right] - \frac{\kappa}{2}\right\}\alpha_2 + \sqrt{\kappa}\alpha^{\mathrm{in}}, \\ \dot{\beta}_1 &= -\left(i\omega_1 + \frac{\gamma_m}{2}\right)\beta_1 + iJ\beta_2 + ig\alpha_1^*\alpha_1, \\ \dot{\beta}_2 &= -\left(i\tilde{\omega}_2 + \frac{\gamma_m}{2}\right)\beta_2 + iJ\beta_1 + ig\alpha_2^*\alpha_2, \end{aligned} \tag{B3}$$

where $\tilde{\omega}_2 = \omega_2 - g_{\mathrm{cK}}\alpha_2^*\alpha_2$ is the optically tunable mechanical frequency mentioned in the main text.

For an overview of the cross-Kerr-effect, we extend Fig. 5(a) to a large-scale parameter space and for different frequency mismatches as shown in Fig. 8. The cross-Kerr-term required both to reach minimal splitting and to get closer to the EP increases as the frequency mismatch increases. This comes from the tuned frequency $\tilde{\omega}_2 = \omega_2 - g_{\mathrm{cK}}\alpha_2^*\alpha_2$, which reveals the usefulness of cross-Kerr-coupling not only in frequency control but also in sensitivity enhancement.

[1] M. Li, H. X. Tang, and M. L. Roukes, Ultra-sensitive NEMS-based cantilevers for sensing, scanned probe and very high-frequency applications, Nature Nanotech. **2**, 114 (2007).

[2] K. L. Ekinci, X. M. H. Huang, and M. L. Roukes, Ultrasensitive nanoelectromechanical mass detection, Appl. Phys. Lett. **84**, 4469 (2004).

[3] N. V. Lavrik and P. G. Datskos, Femtogram mass detection using photothermally actuated nanomechanical resonators, Appl. Phys. Lett. **82**, 2697 (2003).

[4] B. Ilic, H. G. Craighead, S. Krylov, W. Senaratne, C. Ober, and P. Neuzil, Attogram detection using nanoelectromechanical oscillators, J. Appl. Phys. **95**, 3694 (2004).

[5] Y. T. Yang, C. Callegari, X. L. Feng, K. L. Ekinci, and M. L. Roukes, Zeptogram-scale nanomechanical mass sensing, Nano Lett. **6**, 583 (2006).
[6] J. Chaste, A. Eichler, J. Moser, G. Ceballos, R. Rurali, and A. Bachtold, A nanomechanical mass sensor with yoctogram resolution, Nature Nanotech. **7**, 301 (2012).
[7] J.-J. Li and K.-D. Zhu, All-optical mass sensing with coupled mechanical resonator systems, Phys. Rep. **525**, 223 (2013).
[8] J.-J. Li and K.-D. Zhu, Nonlinear optical mass sensor with an optomechanical microresonator, Appl. Phys. Lett. **101**, 141905 (2012).
[9] F. Liu, S. Alaie, Z. C. Leseman, and M. Hossein-Zadeh, Sub-pg mass sensing and measurement with an optomechanical oscillator, Opt. Express **21**, 19555 (2013).
[10] H. Xiong, L.-G. Si, and Y. Wu, Precision measurement of electrical charges in an optomechanical system beyond linearized dynamics, Appl. Phys. Lett. **110**, 171102 (2017).
[11] C. Jiang, Y. Cui, and K.-D. Zhu, Ultrasensitive nanomechanical mass sensor using hybrid opto-electromechanical systems, Opt. Express **21**, 13773 (2014).
[12] Y. He, Sensitivity of optical mass sensor enhanced by optomechanical coupling, Appl. Phys. Lett. **106**, 121905 (2015).
[13] J. Hakansson, B. Kuyken, and D. V. Thourhout, Strong forces in optomechanically actuated resonant mass sensor, Opt. Express **25**, 30939 (2017).
[14] I. M. Haghighi, N. Malossi, R. Natali, G. Di Giuseppe, and D. Vitali, Sensitivity-Bandwidth Limit in a Multimode Optoelectromechanical Transducer, Phys. Rev. Appl. **9**, 034031 (2018).
[15] T. S. Biswas, J. Xu, N. Miriyala, C. Doolin, T. Thundat, J. P. Davis, and K. S. D. Beach, Time-Resolved Mass Sensing of a Molecular Adsorbate Nonuniformly Distributed along a Nanomechnical String, Phys. Rev. Appl. **3**, 064002 (2015).
[16] J. Wiersig, Enhancing the Sensitivity of Frequency and Energy Splitting Detection by Using Exceptional Points: Application to Microcavity Sensors for Single-Particle Detection, Phys. Rev. Lett. **112**, 203901 (2014).
[17] W. Chen, S. K. Özdemir, G. Zhao, J. Wiersig, and L. Yang, Exceptional points enhance sensing in an optical microcavity, Nature **548**, 192 (2017).
[18] H. Hodaei, A. U. Hassan, S. Wittek, H. Garcia-Gracia, R. El-Ganainy, D. N. Christodoulides, and M. Khajavikhan, Enhanced sensitivity at higher-order exceptional points, Nature **548**, 187 (2017).
[19] Z.-P. Liu, J. Zhang, S. K. Özdemir, B. Peng, H. Jing, X.-Y. Lü, C.-W. Li, L. Yang, F. Nori, and Y.-X. Liu, Metrology with PT-Symmetric Cavities: Enhanced Sensitivity near the $\mathcal{PT}$-Phase Transition, Phys. Rev. Lett. **117**, 110802 (2016).
[20] P. Djorwe, Y. Pennec, and B. Djafari-Rouhani, Frequency locking and controllable chaos through exceptional points in optomechanics, Phys. Rev. E **98**, 032201 (2018).
[21] T. K. Paraïso, M. Kalaee, L. Zang, H. Pfeifer, F. Marquardt, and O. Painter, Position-Squared Coupling in a Tunable Photonic Crystal Optomechanical Cavity, Phys. Rev. X **5**, 041024 (2015).
[22] M. Aspelmeyer, T. J. Kippenberg, and F. Marquardt, Cavity optomechanics, Rev. Mod. Phys. **86**, 1391 (2014).
[23] J. D. Cohen, S. M. Meenehan, G. S. MacCabe, S. Gröblacher, A. H. Safavi-Naeini, F. Marsili, M. D. Shaw, and O. Painter, Phonon counting and intensity interferometry of a nanomechanical resonator, Nature **520**, 522 (2015).
[24] S. Hong, R. Riedinger, I. Marinkovic, A. Wallucks, S. G. Hofer, R. A. Norte, M. Aspelmeyer, and S. Gröblacher, Hanbury Brown and Twiss interferometry of single phonons from an optomechanical resonator, Science **358**, 203 (2017).
[25] H. Xu, D. Mason, L. Jiang, and J. G. E. Harris, Topological energy transfer in an optomechanical system with exceptional points, Nature **537**, 80 (2016).
[26] M. Pernpeintner, P. Schmidt, D. Schwienbacher, R. Gross, and H. Huebl, Frequency Control and Coherent Excitation Transfer in a Nanostring-Resonator Network, Phys. Rev. Appl. **10**, 034007 (2018).
[27] H. Fu, Z.-C. Gong, L.-P. Yang, T.-H. Mao, C.-P. Sun, S. Yi, Y. Li, and G.-Y. Cao, Coherent Optomechanical Switch for Motion Transduction Based on Dynamically Localized Mechanical Modes, Phys. Rev. Appl. **9**, 054024 (2018).
[28] N. R. Bernier, L. D. Tóth, A. K. Feofanov, and T. J. Kippenberg, Level attraction in microwave optomechanical circuit, Phys. Rev. A **98**, 023841 (2018).
[29] K. Fang, M. H. Matheny, X. Luan, and O. Painter, Optical transduction and rounting of microwave phonons in cavity-optomechanical circuits, Nat. Photonics **10**, 489 (2016).
[30] J. Chan, A. H. Safavi-Naeini, J. T. Hill, S. Meenehan, and O. Painter, Optimized optomechanical crystal cavity with acoustic radiation shield, Appl. Phys. Lett. **101**, 081115 (2012).